Microstructural considerations of enhanced tensile strength and mechanical constraint in a copper/stainless steel brazed joint

Li, Y., Parfitt, D., Flewitt, P. E. J., Hou, X., Quinta de Fonseca, J. & Chen, B.
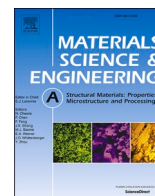
Microstructural considerations of enhanced tensile strength and mechanical constraint in a copper/stainless steel brazed joint

Y. Li [a],[**], D. Parfitt [a], P.E.J. Flewitt [b], X. Hou [c], J. Quinta de Fonseca [d], B. Chen [a],[e],[*]

[a] The Institute for Future Transport and Cities, Coventry University, Coventry, CV1 5FB, UK
[b] H.H. Wills Physics Laboratory, University of Bristol, Bristol, BS8 1TL, UK
[c] Centre of Excellence for Advanced Materials, Dongguan, 523808, China
[d] Material Science Centre, University of Manchester, Manchester, M13 9PL, UK
[e] School of Engineering, University of Leicester, Leicester, LE1 7RH, UK

ABSTRACT

The microscopic and macroscopic material strengthening mechanisms encountered in brazed joints were experimentally investigated and quantified in this work. Microstructural contribution towards the overall strength of a stainless steel brazed joint was evaluated by conducting multi-scale microstructural characterisations. Theoretical evaluation of the collected microstructural data suggests a Cu–Mn solid-solution strengthening enhancement of ~200 MPa towards the overall joint strength. The mechanical constraint effect was considered as the macroscopic strengthening mechanism, as revealed by comparing two identical joints but with their interfaces orientated at 90° and 45° with respect to the applied load. Bridgman necking criteria was applied to derive the longitudinal flow stress for the 90° joint configuration. The discrepancy (~330 MPa) between the calculated and experimentally determined strengths can thus be concluded as the contribution of mechanical constraint. In addition, the pile-up of geometrically necessary dislocations (GNDs) was observed at the base-filler metal interface for the 90° joint, but a homogeneous GND distribution was revealed for the 45° one. This observation indicates that GNDs were introduced to accommodate deformation incompatibility imposed by the mechanical constraint. This finding is thus considered as an experimental (microscopic) evidence for strain inhomogeneity due to the presence of mechanical constraint.

1. Introduction

High-temperature brazing is a reliable approach to produce joints with appropriate mechanical performance. Copper is widely adopted as filler material for brazing stainless steel due to its favourable wetting behaviour [1]. In addition, the magnitude of thermal residual stress is limited because of the similar coefficient of thermal expansion between these two materials. Experimental evidence [2,3] showed that copper brazed steel joints had enhanced tensile strength when compared to the bulk filler material. For example, Kavishe and Baker [3] brazed Ni–Cr–Mo low-alloy steel with copper and it was found that the tensile strength of the brazed joint was three times that of the filler material. To our knowledge, the strength enhancement of brazed joints was almost exclusively attributed to the mechanical constraint of the base metal [4, 5].

Upon tensile loading, the plastic flow of brazed joint was laterally restricted by the base metal due to material property mismatch, resulting in a triaxial stress state within the joint region [4]. Such a triaxiality was claimed to be the reason for the increased tensile strength of the joint. Additionally, West et al. [5] found that the interfacial shear stress at the base-filler metal interface increased as the joint thickness decreased, causing extra restriction on joint deformation. This implies that the mechanical constraint can be changed with different joint designs. The term "mechanical constraint" is frequently adopted to explain the enhanced mechanical strengths for brazed joints [6], but without a mechanistic-based justification. In addition, previous investigations provided neither a quantitative evaluation of stress triaxiality nor the influence of brazed joint microstructures. Thus, the strengthening mechanism as well as the plastic flow of brazed joints deserve further theoretical analysis together with experimental verification.

This paper presents multi-scale microstructural characterisations of the brazed joint by using a range of complementary tools. Theoretical calculation of the joint strength based on the microstructural data as well as the Bridgman necking criteria was performed to correlate with the experimentally obtained value. Furthermore, braze assemblies were designed to create two joint configurations with their interfaces orientated at 45° and 90° with respect to the loading direction. The design of 45° joint in principle would help to reduce the influence of mechanical constraint when compared to the 90° joint. This would then enable a direct comparison of the plastic flow capability and the overall strength of brazed joints under different mechanical constraint levels.

Besides the macroscopic strengthening effect, microscopic aspect of the mechanical constraint is also of interest. Studies demonstrated that electron backscatter diffraction (EBSD) can be used as a reliable technique for characterising dislocation densities close to interfaces at micrometre scale. For example, Kadkhodapour et al. [7] performed an experimental study of geometrically necessary dislocations (GNDs) within dual phase steels where GNDs close to the ferrite-martensite phase boundaries was one order of magnitude higher than those at grain interiors, causing local strain hardening. In addition, Jiang et al. [8] studied the evolution of GNDs in copper during tensile loading by using EBSD combined with cross-correlation. According to the investigations above, interrupted tensile tests were conducted on the 45° and 90° brazed joints in the current work. This was followed by post-mortem EBSD analysis, as a new approach for plastic flow characterisation, to investigate dislocation characteristics as well as GND distribution within the brazed joints. The deformation incompatibility in the vicinity of the base-filler metal interface is thus experimentally revealed for the first time.

2. Material and experiment

2.1. Fabrication of brazed joints with 90° and 45° orientations

Type 304 stainless steel (Rapid Metals, UK), abbreviated as SS, was selected as the base metal. Copper foil of 125 μm thick (Alfa Aesar, Thermo, UK) was used as the filler material. The chemical composition of the SS is 9.25Ni, 19.00 Cr, 2.00 Mn, 1.00 Si and Fe in balance (all in wt.% unless otherwise specified), and the as-supplied copper is 99.99% pure. Prior to brazing, bonding surfaces of the SS were prepared using P180-grade SiC papers to ensure satisfactory wetting. This was followed by degreasing and cleaning with acetone in an ultrasonic bath for 10 min. Fig. 1(a) and (b) show the brazed joint assembly design together with specimen extraction for performing uniaxial tensile tests and microstructure characterisation. Copper foil was inserted in between the SS pieces, at 90° and 45° orientations with respect to the loading

direction. The design of 45° joint aimed at promoting a shear-type of failure as the maximum in-plane shear stress is inclined at 45° in respect to the tension axis. Thus, the 45° joint configuration would plastically deform in shear under a reduced level of mechanical constraint (i.e. a low stress triaxiality) as compared to the 90° counterpart. As demonstrated in previous work [9,10], stress triaxiality levels of axisymmetric tensile specimens, angled at 30°–45° with respect to the far-filed loading axis, were much reduced as compared to that of 90°.

Brazing was performed in a conveyor belt furnace at 1120 °C under a hydrogen atmosphere for approx. 1 h. During the heating stage, the temperature increased from 200 °C to 1080 °C within 6 min, followed by increasing to 1120 °C and held at this temperature for 10 min. This was followed by furnace cooling to room temperature within 30 min. Details of the joint assembly and brazing process can be found in Ref. [11].

After brazing, the central portion of the as-brazed joint assembly was extracted by electrical-discharge-machining (EDM) to acquire dog-bone profiles, as indicated in Fig. 1(a) and (b). The extracted dog-bone assembly was sliced into flat tensile test specimens of 3 mm thickness; the specimen dimension is shown in Fig. 1(c). After specimen extraction, the remaining joint assembly was used for microstructural characterisation and the sampling location is indicated by the rectangular box in Fig. 1 (d). The extracted rectangular block was sliced into multiple pieces, Fig. 1(d), and at least five different regions were examined to obtain statistically significant information about the joint microstructure.

2.2. Tensile testing and nanoindentation

The tensile test specimens had a parallel gauge length of 10 mm and a width of 6 mm, Fig. 1(c). Uniaxial tensile tests were performed on an Instron 8802 servo-hydraulic testing system at room temperature with a constant strain rate of $3.3 \times 10^{-4}\,s^{-1}$. The axial strain was measured by using clip-on extensometer with a gauge length of 10 mm and travel distance of ± 1 mm. Three specimens per joint design (90° and 45° orientations) were tensile loaded to failure and the average property was derived. In addition, interrupted tensile tests were performed and the specimens were loaded up to 90% of the final fracture stress.

Berkovich nanoindentations were obtained using a Zwick/Roell ZHN instrumented indentation system to reveal the strength heterogeneity within the brazed joint including regions in the vicinity of the base-filler metal interface. Positioning of the indentation was controlled with an optical microscope and an array of 10 × 5 indents were tested. Nanoindentation was conducted using force control with a constant indentation depth. The indentation force was set to be 3.5 mN as this resulted in the indent size being in the range of 2 μm–5 μm [12]. The spacing between each individual indent was set as 15 μm (5 times the indent size) to avoid interference from the plastic zone of neighbouring indents.

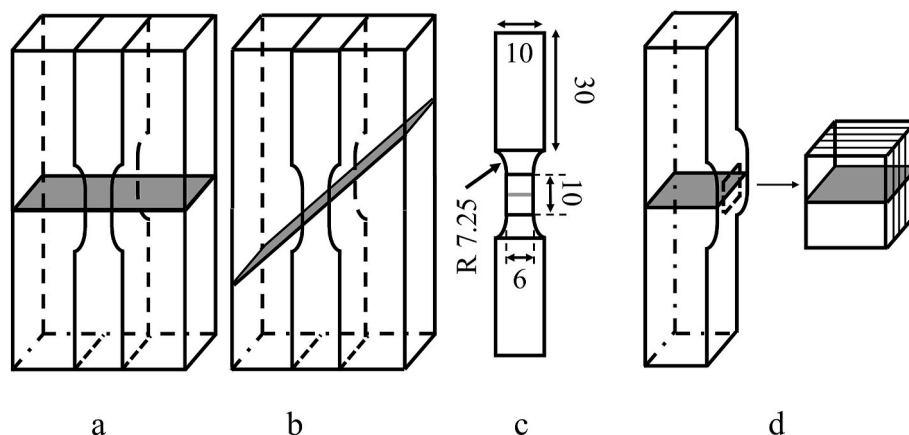

Fig. 1. Brazed joint configurations with respect to the tensile loading direction: (a) 90°; (b) 45°; (c) dimensions of tensile test specimen in mm; (d) sampling location for microstructure characterisation and extracted rectangular specimen.

The hardness was derived as a function of the depth of each indent using the Oliver-Pharr method [13].

2.3. Microstructure

Joint microstructure characterisation was performed on the basis of the 90° joint configuration, Fig. 1(d). A standard metallographic sample preparation procedure was followed, that included sequentially grinding to P1200, polishing to a finish of 1 μm, and finally OPS polishing using a vibro-polisher for 12 h with 0.02 μm colloidal silica to achieve a nominal deformation-free surface [14]. Microstructure of the brazed joint was revealed using a Zeiss Gemini scanning electron microscope (SEM) at 15 kV under the backscattered electron (BSE) imaging mode. Texture and grain size measurements were conducted using EBSD on a JEOL JSM-7200F SEM at 15 kV with 1 μm step size. High-magnification SEM images were collected and processed using ImageJ to obtain the size, distribution and volume fraction of second phase particles based on 500 measurements.

SEM fractography was performed to evaluate the failure mechanism. The interrupted tensile specimens were subjected to longitudinal cross-section and metallographic preparation, followed by SEM observation and EBSD scans to reveal the plastic flow characteristics. A field-of-view of 250 × 150 μm^2 at a step size of 0.25 μm was used for EBSD scan to ensure an appropriate spatial resolution. Measuring the location-specific crystallographic orientations enables the calculation of lattice curvature, from which the GND density can be derived using the Nye dislocation density tensor [15,16].

To reveal the crystal structure of second phase particles within the brazed joint, a JEOL JEM-3000F transmission electron microscope (TEM), operated at 200 kV was used for imaging and selected area electron diffraction (SAED). In addition, an atomic-resolution JEOL ARM-200F Cs corrected S/TEM, equipped with a highly efficient (Centurion) energy dispersive X-ray (EDX) system, was used for elemental analysis and atomic-scale characterisation in STEM mode (operated at 200 kV). The probe size was set to 0.1 nm with a convergence semi-angle of 22.5 mrad. The collection angle of the high angle annular dark field (HAADF) detector was in the range of 80–150 mrad.

In-situ lift-out TEM sample preparation was conducted by using a focused ion beam (FIB) workstation (Zeiss Gemini 2 FIB/SEM crossbeam 540) equipped with a micro-manipulator. Ga$^+$ ions accelerated at 30 kV were used for milling and polishing with FIB currents in descending order from 65 nA, 15 nA, 7 nA–3 nA, Fig. 2(a). This was followed by FIB lift-out and attachment to a copper grid by using 200 pA current to minimise the damage. The TEM sample was then cleaned at 700 pA, 300 pA and 100 pA at 30 kV, followed by final polish at 200 pA, 2 kV, Fig. 2 (b). More details about FIB milling and polishing can be found elsewhere [17]. SAED patterns were processed using Digital Micrograph 3.5 and Gatan Microscopy Suite 2.1 to acquire lattice constants for both the copper matrix and second phase particles. In addition, orientation relationship between the second phase particles and the copper matrix was determined from the collected STEM-HAADF images by applying fast Fourier transform (FFT).

3. Results

3.1. Microstructure

3.1.1. Grain size and texture

The overall microstructure of the stainless steel brazed joint is shown in Fig. 3(a), where the brighter region was the copper-based joint and darker region was the base stainless steel. No cracks or porosities were observed at the base-filler metal interface, implying good wetting behaviour. The thickness of the brazed joint was ~110 μm, which agrees well with the thickness of 125 μm for the inserted copper foil. A representative EBSD orientation map for the brazed joint region is shown in Fig. 3(b), revealing an equiaxed grain structures. The grains within the joint region were randomly orientated with intensities less than 4 times the perfect isotropic case for the {100} pole figure, Fig. 3(c), suggesting the presence of a weak texture. The grain size is shown in Fig. 3(d) where the size-distribution histogram and the Weibull fit curve are presented. The average grain size (equivalent diameter) was determined as 57.2 ± 2.3 μm by examining over 500 grains. The 45° brazed joint had similar equiaxed grains, weak texture, and an average grain size of 60.3 ± 7.2 μm (for brevity, results are not shown in this work). Fig. S1 in the supplementary material provides a direct comparison of joint microstructures between the 90° and 45° configurations.

3.1.2. Precipitation

Fig. 4(a) shows detailed joint microstructure at the as-brazed condition where individual grains, grain boundaries as well as the base-filler metal interface (indicated by white arrows) can be seen. The presence of star-shaped precipitates within the joint region were revealed at higher magnification and shown in the inset in Fig. 4(a). It is also confirmed that these precipitates existed in each individual grain throughout the brazed joint. In addition, both the size and number density of the precipitates decreased in the vicinity of grain boundaries, Fig. 4(b), which is consistent with a precipitate-free zone theory [18]. The size of the precipitates was similar at all positions within grain interiors. Their average size and volume fraction were determined to be 117 ± 25 nm (radius) and 2.3%, respectively. Ghovanlou et al. [6] conducted brazing of low carbon steels using copper where iron-rich precipitates with a similar morphology were found. Under the thermodynamic equilibrium condition, copper can dissolve up to 3.5 wt% iron at the brazing temperature of 1120 °C, whereas the solubility of iron in copper at room temperature is negligible. Therefore, these star-shaped features are likely to be iron-rich copper precipitates.

A representative TEM bright-field (BF) image of precipitates in the brazed joint is shown in Fig. 5(a). Based on the SAED patterns ([01$\bar{1}$] zone axis) for the precipitate in Fig. 5(b) and the copper matrix in Fig. 5 (c), it is evident that the star-shaped precipitate has the same crystal structure to the copper matrix, i.e. face-centred cubic (fcc). However, the lattice constants of the precipitates and the copper matrix were
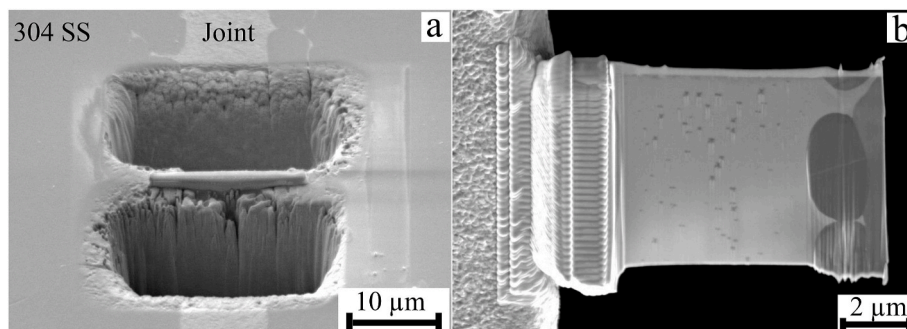

Fig. 2. (a) FIB TEM lamella position relative to the brazed joint; (b) TEM lamella after final polish.
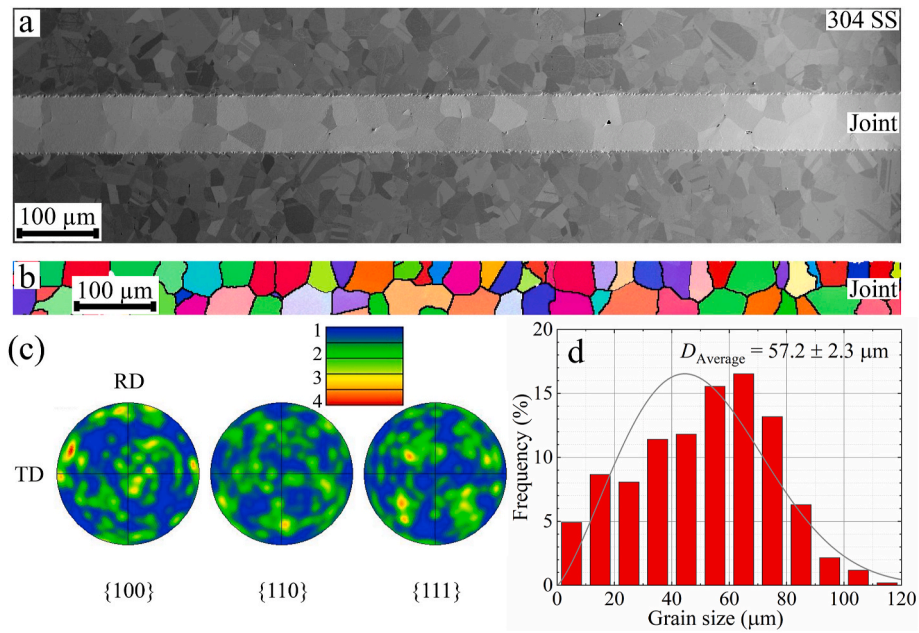
Fig. 3. (a) SEM image of the as-brazed joint microstructure; (b) corresponding EBSD orientation map, showing near equiaxed grains within the joint region; (c) pole figures indicating a relatively weak texture; (d) grain size-distribution (equivalent diameter).

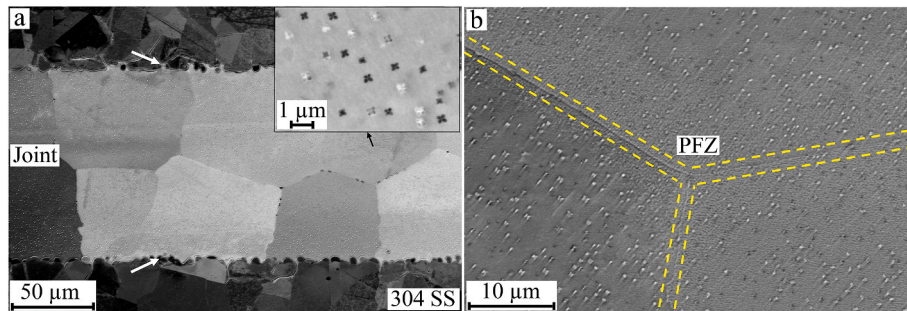**Fig. 4.** (a) Brazed joint microstructure showing individual grains as well as grain boundaries; the inset illustrates the star-shaped precipitates within individual grains; (b) precipitate-free zone (PFZ) in the vicinity of grain boundaries.
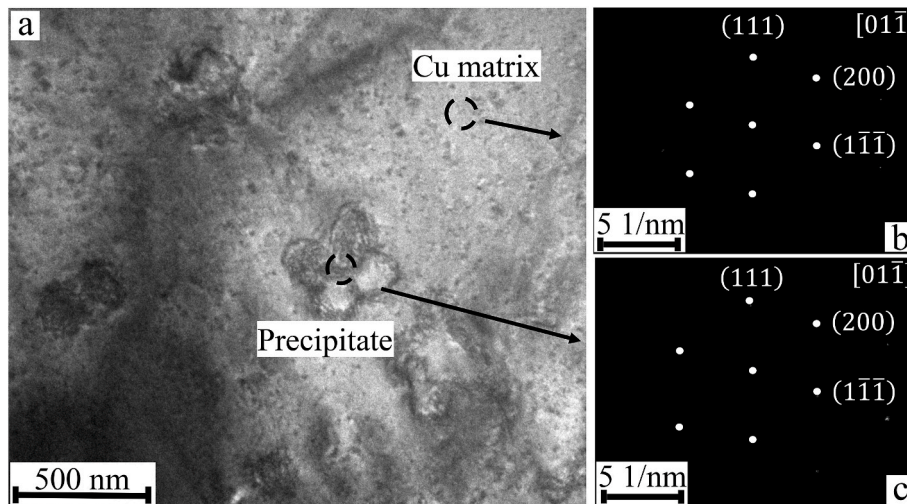

Fig. 5. (a) Bright-field TEM image along the $[01\bar{1}]$ zone axis; (b) selected area electron diffraction (SAED) pattern of the copper-rich matrix; (c) SAED pattern of the precipitate.

determined to be 0.361 nm and 0.374 nm, respectively. This suggests a lattice constant misfit, $\delta_{\text{matrix-precipitate}}$, of ~5.0% between the two.

To further characterise these precipitates, STEM-HAADF imaging was used and the result is shown in Fig. 6(a). The two insets reveal the atomic arrangements of the copper matrix and the precipitate, Fig. 6(b) and (c), respectively. Interplanar spacings of both the (111) and (200) planes were measured, and the results showed that the precipitate had smaller interplanar spacings when compared to the copper matrix. Fig. 6 (d) shows the interfacial region between the precipitate and the copper matrix. It can be seen from the corresponding FFT pattern, Fig. 6(e), that the precipitate and the matrix had a highly coherent interface with the orientation relationship of $(111)_{\text{matrix}}$// $(111)_{\text{precipitate}}$, $(1\overline{1}1)_{\text{matrix}}$// $(1\overline{1}1)_{\text{precipitate}}$ and $(200)_{\text{matrix}}$// $(200)_{\text{precipitate}}$. This observation is consistent with the study by Chen et al. [19] on 150 nm fcc-structured star-shaped precipitates in Cu–10Sn–2Zn-1.5Fe-0.5Co alloy. The morphology of the star-shaped precipitate was claimed to be associated with the balance between the precipitate/matrix interfacial energy and coherent strain energy, with the primary branch growing preferentially along the <111> directions [20,21].

3.1.3. Composition

STEM-EDX elemental mapping of the precipitates is presented in Fig. 7(a)-7(f). It is evident that manganese, Fig. 7(f), was homogeneously distributed throughout the copper joint region, whereas amounts of chromium, iron and nickel, Fig. 7(b), (c) and (e), were location dependent and concentrated at the precipitates. Thus, the star-shaped precipitates were enriched in chromium, iron and nickel while relatively depleted in copper when compared to the matrix, Fig. 7(d). Furthermore, STEM-EDX point analysis was performed to obtain a semi-quantitative evaluation of the elemental distribution; the results were based on the average of five measurements. The copper matrix contained $5.9 \pm 0.1\%$ Ni, $2.9 \pm 0.1\%$ Fe, $1.9 \pm 0.1\%$ Mn, $0.6 \pm 0.1\%$ Cr and 88.7% Cu (all in wt.% unless otherwise stated), whereas the precipitates contained $16.9 \pm 3.3\%$ Ni, $39.8 \pm 10.8\%$ Fe, $1.9 \pm 0.1\%$ Mn, $8.0 \pm 1.3\%$ Cr and 33.4% Cu. In discussion section, we will use this elemental information to derive the contributions to the overall tensile strength of the brazed joint.

3.2. Mechanical properties

3.2.1. Nanoindentation

Nanoindentation was performed to evaluate strength heterogeneity across the brazed joint. Fig. 8(a) shows locations of the 10 indents in the base stainless steel (5 indents on each side), 10 within the brazed joint but close to the base-filler metal interface, and the rest being distributed within the joint. Each row of the indents covered the entire joint region with the first and last being in the base metal. The average indent size in the SS was 2.0 μm, which was smaller than those within the brazed joint of 2.5 μm, Fig. 8(a). This difference in indent size corresponds well with the determined hardness, i.e. the SS had a hardness value well above 2.5 GPa while those in the brazed joint were below 1.5 GPa, Fig. 8(b). Note any indent positioned close to the interface or a free surface (e.g. less than a distance of 3 times the indent diameter) is judged inappropriate according to the best practice of performing quantitative and reproducible indentation measurement [22]. As a result, no attempt was made to capture the refined hardness profile across the interface.

The average hardness of the copper matrix in the central region of the brazed joint was 1.1 GPa, Fig. 8(b), and this was significantly higher than those being reported for pure copper of 0.5–0.7 GPa [22,23]. Taking indentation size effect into consideration, the obtained hardness of 1.1 GPa was still higher than that of single-crystal copper (0.7 GPa for a {110} crystallographic plane) obtained with a similar Berkovich indent size [12]. Hall-Petch effect can also affect the indentation hardness measurement, but it would require an average grain size of 1.2 μm for pure copper to achieve such a high hardness value of 1.1 GPa [12, 22]. This is significantly smaller compared to the 57.2 ± 2.3 μm observed in Fig. 3(d). Moreover, regions in the vicinity of the base-filler metal interface showed a further hardness increase to 1.3 GPa (circled in Fig. 8(b)). We will discuss this interesting aspect in detail together with the measured GND density in section 4.3.

3.2.2. Tensile strength of 90° and 45° joints

The engineering stress-strain curves of the 90° and 45° brazed joints are presented in Fig. 9. The corresponding 0.2% offset yield stress, σ_y, fracture stress, σ_f, as well as elongation-to-failure strain, ε, are summarised in Table 1. Tensile properties of polycrystalline copper as well as precipitation-hardened copper obtained from the literature are also listed in Table 1 for comparison. The 90° brazed joint had a fracture stress of 478.7 ± 4.2 MPa and elongation-to-failure strain of $15.4 \pm 0.3\%$. The fracture surface, as shown in the inset (a) in Fig. 9, revealed
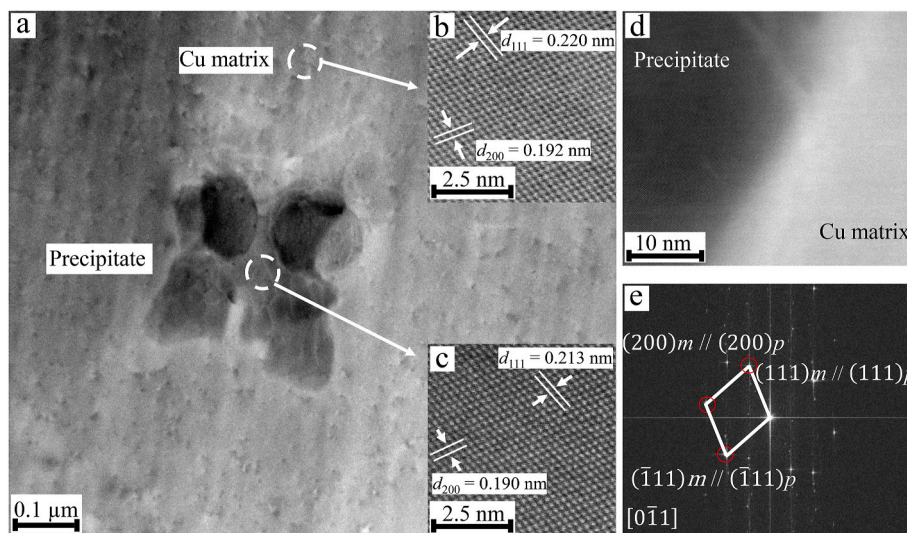

Fig. 6. (a) HAADF imaging of a precipitate; (b) atomic arrangement of the copper matrix; (c) atomic arrangement of the precipitate; (d) high-resolution TEM image showing the interfacial region between the precipitate and the copper matrix; (e) FFT pattern of the interfacial region in (d), indicating the orientation relationship between the star-shaped precipitate and the copper matrix.
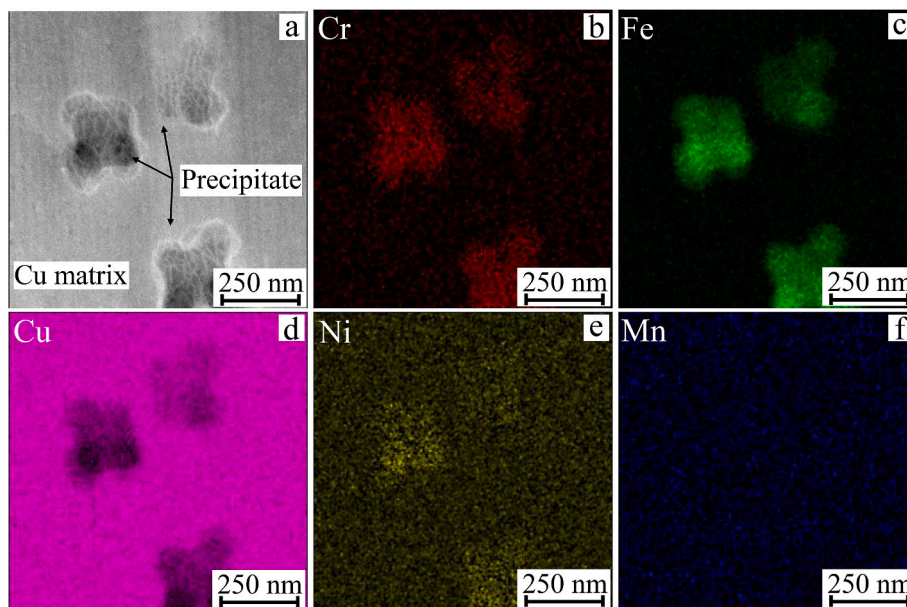
Fig. 7. (a) HAADF imaging of star-shaped precipitates; (b) to (f) STEM-EDX element mapping.
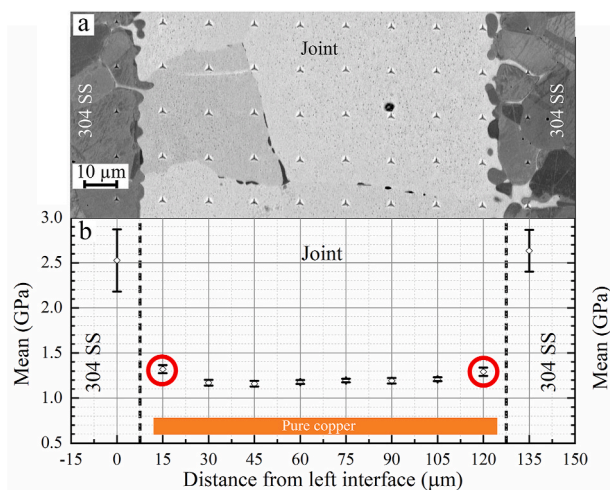

Fig. 8. (a) The array of Berkovich indents across the brazed joints; (b) hardness derived from the nanoindentation measurements with the colour band representing hardness values for pure copper [22]. (For interpretation of the references to colour in this figure legend, the reader is referred to the Web version of this article.)

equiaxed dimples with sizes ranging from 30 μm to 100 μm, suggesting a ductile fracture mode. Overall, the 90° brazed joint exhibited enhanced tensile strength (both σ_y and σ_f) when compared to the filler metal (i.e. polycrystalline pure copper), Table 1. This observation is consistent with the nanoindentation results, Fig. 8(b). Note that a positive linear relationship exists between the yield strength and hardness [24]. But the determination of yield strength based on nanoindentation hardness needs to consider both the indentation size effect and strain hardening coefficient. A correlation between the two for the brazed joint is beyond the scope of the current work.

The 45° brazed joint had a fracture stress of 385.6 ± 8.5 MPa with elongation-to-failure strain of 10.6 ± 0.9%, being ~20% lower than the 90° counterpart, Table 1. The yield strength of 206 ± 0.1 MPa was also lower than that of 226 ± 0.1 MPa for the 90° counterpart, Fig. 9. The strain values reported in Fig. 9 included elongations of the stainless steels and the brazed joints as a 10 mm gauge section was measured.

SEM fractography revealed elongated dimples, indicating a shear-failure mode, inset (b) in Fig. 9. Since the joint microstructures were identical for the 90° and 45° configurations, Fig. 3, the lower tensile strength of the 45° joint can be attributed to the reduced mechanical constraint effect.

3.2.3. Plastic flow characteristics

Fig. 10 (a) and 10(d) present SEM-BSE images for the 90° and 45° joints strained to 90% of the fracture stress (~430 MPa and ~345 MPa, respectively, Table 1), and the viewing direction is indicated in Fig. 9. It was found that dislocation contrast selectively appeared at certain grains in the 90° joint, Fig. 10 (a), suggesting a preferred slip occurring with respect to the active slip systems. By comparison, dislocation contrast was uniformly distributed for the 45° counterpart, indicating homogeneous plastic deformation. Fig. 10(b) and (e) reveal the deformation characteristics within individual grains of the 90° and 45° joint configurations where the banded structures are present. Higher-magnification SEM images reveal the formation of extended boundaries within the banded structures, Fig. 10(c) and (f). These boundaries are characteristics of dislocation cell block structures as their appearance is a consequence of accommodation of slip system differences [26]. TEM observation of similar dislocation structures [26–28] confirmed these two types of boundaries, i.e. geometrically necessary boundaries (GNBs) that separate the cell block structures and incidental dislocation boundaries (IDBs) defining equiaxed volumes in between the GNBs [29]. This is illustrated in Fig. 10(c) and (f) where the solid yellow lines represent the GNBs and the dotted lines (in between solid yellow lines) denote IDBs.

The GNB spacings of the 45° and 90° joints were measured and the average value was reported; this was determined from more than 100 cell block structures across multiple grains. As representatively demonstrated in Fig. 10(c) and (f), GNB spacing in the 45° joint (0.33 ± 0.15 μm) was smaller than the 90° counterpart of 0.43 ± 0.15 μm. According to the evolution theory for dislocation cell block structures [30], new GNBs would always form preferentially within thicker cell block structures. This would allow subdivision of cell block structures to accommodate additional lattice curvature, hence reducing the overall GNB spacing. In addition, Mishin et al. [31] reported that GNB spacing would decrease with increased plastic strain, while misorientations across them increase. Hence, the smaller GNB spacing indicates a higher strain level for the 45° brazed joint. Since the 90° and 45° joints were
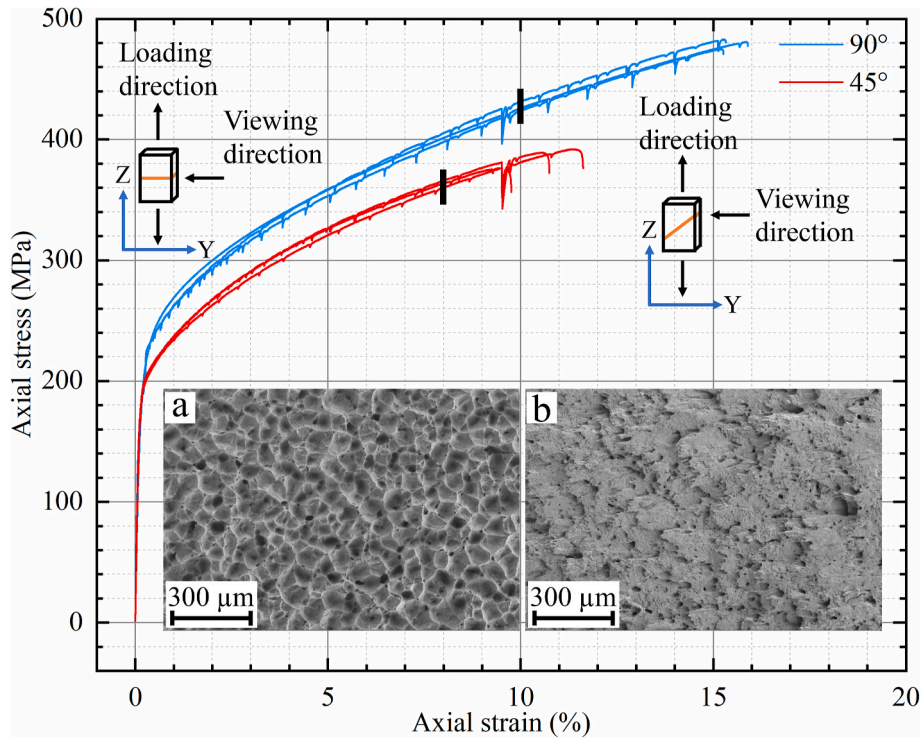
Fig. 9. Axial stress-strain curves of the 90° and 45° brazed joint. Insets (a) and (b) show representative fracture surfaces of the 90° and 45° joint configurations, respectively.

Table 1
Tensile properties of the 90° and 45° brazed joint configurations.

Material	σ_y (MPa)	σ_f (MPa)	ε (%)	90% of σ_f (MPa)
90° brazed joint	226 ± 0.1	478.7 ± 4.2	15.4 ± 0.3	~430
45° brazed joint	206 ± 0.1	385.6 ± 8.5	10.6 ± 0.9	~345
Polycrystalline pure copper [25]	~50	~200	32.4	N/A

subjected to 90% of the corresponding fracture stresses (~430 MPa and ~345 MPa, respectively), the 45° joint thus showed a higher strain level at a lower applied stress. This finding substantiates that the 45° brazed joint was less constrained when compared to the 90° counterpart.

Fig. 11 shows EBSD orientation maps of the 90° and 45° joints, with Fig. 11(a) and (b) for the as-brazed (i.e. no-stress) condition, while Fig. 11(c) and (d) are for the strained condition. The macroscopic base-filler metal interfaces are indicated by arrows. The EBSD measurement noise increased with the increasing plastic strain due to the lattice distortion induced by the increase in dislocation density, i.e. indexing success rate [28]. Nevertheless, greater than 90% indexing success rate was always achieved for the heavily strained specimens in the present work. This made the subsequent detailed GND analysis reliable. The black dots within individual grains in Fig. 11(a) and (b) corresponded to the star-shaped precipitates that cannot be resolved by EBSD. The high angle grain boundaries (HAGBs, > 15°, thick red lines) and low angle grain boundaries (LAGBs, between 2° and 15°, thin black lines) for both joint configurations are also indicated in Fig. 11. The presence of local strain gradient for both the 90° and 45° joints after being strained to 90% of the fracture stress, Fig. 11(c) and (d), were revealed by the large degree of misorientation induced lattice curvature. For the as-brazed joints, few LAGBs were found in the 90° and 45° joints, Fig. 11(a) and (b), respectively. LAGBs were found at certain grains in the 90° joint, Fig. 11(c), suggesting a preferred slip occurring with respect to the

active slip systems. In contrast, uniform distribution of LAGBs were observed for the 45° joint configuration. The regions with dense LAGBs highlighted by dashed circles in Fig. 11(c) and (d) corresponded to the cell block structures observed in Fig. 10(c) and (f). This observation supports that cell block structures were developed to accommodate different active slip systems, and the extended boundaries of the cell block structures were associated with large degrees of misorientation [32].

4. Discussion

4.1. Microstructure contribution to joint strength

Strengthening mechanisms in polycrystals can be summarised into four categories: solid-solution strengthening, grain size strengthening, dislocation strengthening, and precipitation hardening [33]. For precipitation hardening, the presence of the fine precipitates in metal matrix hinders dislocation motion and results in strengthening. The strengthening effect mainly depends on size, distribution, volume fraction, and strain field associated with the precipitates [34]. Two primary strengthening mechanisms are introduced to describe the interaction between dislocations and precipitates in copper alloys, i.e. dispersion strengthening [35] and coherency strain hardening [36].

Dispersion strengthening assumes that the precipitates do not deform with the matrix. Additional shear stress is needed to allow dislocations to by-pass the precipitates [37]. For the homogenously distributed precipitates within the joint region, Fig. 4(a) and (b), the strengthening by dislocations looping the precipitates can be calculated using the Orowan equation [38]:

$$\sigma_{Orowan} = \frac{0.84MGb}{2\pi(1-\nu)^{1/2}\lambda}\ln\frac{r}{b} \tag{1}$$

where G and b are shear modulus of 45 GPa and Burgers vector of 0.255 nm for copper. $M = 3.06$ is the Taylor factor for fcc polycrystals [39]. $\nu = 0.33$ is the Poisson's ratio and λ is the interparticle spacing between
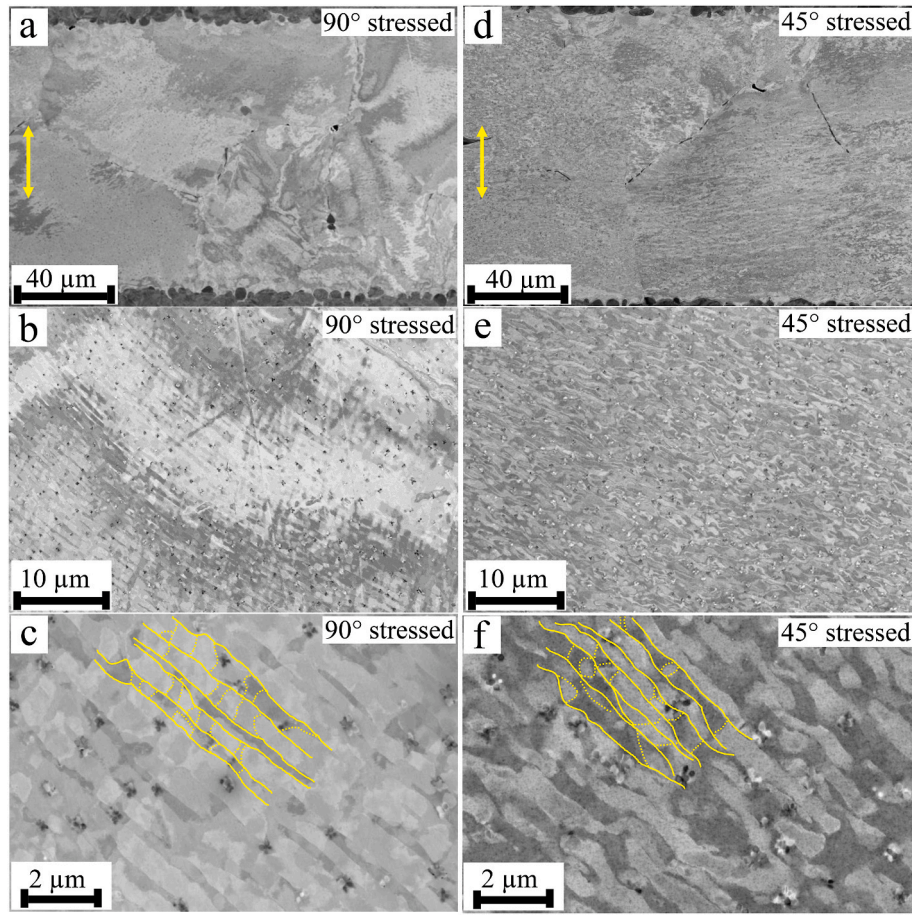
Fig. 10. SEM-BSE images of brazed joints strained to 90% of the fracture stress, (a) to (c) 90° joint configuration; (d) to (f) 45° joint configuration. The loading direction is indicated by yellow arrows in (a) and (d). (For interpretation of the references to colour in this figure legend, the reader is referred to the Web version of this article.)
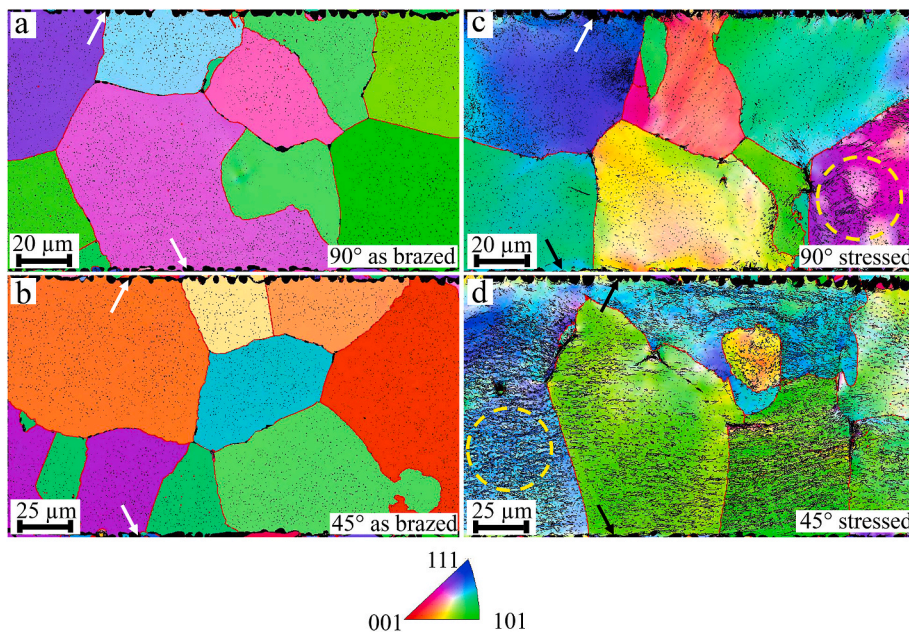

Fig. 11. (a) and (b) EBSD orientation maps (IPF-Z where Z-direction is inwards the paper) of 90° and 45° joint configurations at as-brazed condition; (c) 90° and (d) 45° brazed joints that had been strained to 90% of the fracture stress. High angle grain boundaries (>15°) are indicated in thick red lines and low angle grain boundaries (between 2° and 15°) are shown in thin black lines. (For interpretation of the references to colour in this figure legend, the reader is referred to the Web version of this article.)

the precipitates. To simplify the calculation, the precipitates were treated as spheres with average radius r of 117 nm λ was taken as r $(2\pi/3f)^{0.5}$ [38], where f is the volume fraction of the precipitates (2.3%).

The values of r and f were determined from at least five SEM images similar to the one shown in Fig. 4(a). Consequently, strengthening induced by the dispersed precipitates σ_{Orowan} was calculated to be ~30

MPa.

Based on the high-resolution TEM observations, Fig. 6(d) and (e), it is evident that a cube/cube crystallographic relationship existed between the precipitates and the matrix. The lattice constant misfit $\delta_{matrix-precipitate}$ was estimated as 5.0% by analysing the interplanar spacings of the precipitates for the $[01\bar{1}]$ zone axis of the matrix, Fig. 5(b) and (c). The misfit of lattice constant would produce a local strain field surrounding the precipitates. Although the precipitates (117 ± 25 nm) in this work are much larger than those encountered in conventional precipitation-hardened alloys, Sengupta et al. [40] reported that coherency strain hardening could remain effective for precipitates with sizes up to 1.1 μm. The strengthening as a result of coherency strain hardening $\sigma_{Coherency}$ can be evaluated according to Ref. [41]:

$$\sigma_{Coherency} = 0.7 M G f^{1/2} \left(\frac{2\delta_{matrix-precipitate} 3b^3}{3r^3} \right)^{1/4} \qquad (2)$$

where all the symbols have been defined earlier. $\sigma_{Coherency}$ from the strain field of the precipitate was calculated to be ~60 MPa. However, the precipitation related strengthening mechanism (dislocation-pinning and coherency strain hardening) cannot provide a reasonable explanation to the enhanced fracture stress σ_f (478.7 ± 4.2 MPa, Table 1) in the copper brazed joint.

Grain size strengthening could also contribute towards the enhanced fracture stress. The Hall-Petch relationship relates the yield stress and polycrystal grain size via an inverse square root of dimension [12]:

$$\sigma_y = \sigma_0 + \frac{k}{\sqrt{d}} \qquad (3)$$

where k is a constant, σ_0 and σ_y are the yield strength of single and polycrystal metals, respectively, and d is the mean grain size. To assess the contribution of grain size strengthening, k of 0.1 GPa·$\sqrt{\mu m}$ [22,42] was applied to give an enhancement of ~10 MPa. Therefore, this strengthening mechanism did not account for the fracture stress enhancement.

The SAED results in Fig. 5(b) and (c) reveals that the lattice constant of the copper matrix (0.374 nm) was larger than that of pure fcc copper (0.361 nm), suggesting a solid-solution effect with lattice distortion due to the presence of solute elements. In addition, the STEM-EDX results in Fig. 7 shows small amounts of iron, chromium, nickel, and manganese within the copper matrix. Hence the matrix can be treated as a solid-solution of copper with iron, chromium, nickel and manganese being the solute elements. Therefore, a classical model for substitutional solid-solution strengthening based on elastic dislocation solute interactions [33] was applied:

$$\sigma_{ss} = \frac{M G \delta_{ss}^{3/2} c^{1/2}}{700} \qquad (4)$$

where c is the molar ratio of the solute elements in the copper matrix. The interaction parameter δ_{ss} can be simplified as $\delta_{ss} = |3\delta_{matrix-solute}|$ [43,44]. $\delta_{matrix-solute}$ is the lattice constant misfit between the copper matrix and corresponding solute element. For example, the lattice constant misfit $\delta_{matrix-Fe}$ was calculated as 23.3% by adopting the lattice constant of 0.374 nm for copper matrix (SAED, Fig. 5(b)) and 0.287 nm for iron, respectively. Thus, solid-solution strengthening due to the presence of iron (converted molar ratio $c = 3.3\%$) was ~20 MPa. Similarly, solid-solution strengthening induced by chromium, nickel and manganese would be ~10 MPa, ~3 MPa and ~200 MPa, respectively. In this specific case, the enhancement caused by manganese solid-solution strengthening plays a vital role in enhancing the fracture strength of the copper/stainless steel brazed joint.

Taking the fracture strength of polycrystal copper as ~200 MPa, Table 1, the theoretical fracture strength of the brazed joint can be predicted as ~400 MPa when adding the Cu–Mn solid-solution contribution linearly. However, this theoretically calculated material strength

is still lower than the experimentally derived σ_f of 478.7 ± 4.2 MPa, Table 1. Hence, the microstructural contribution alone cannot explain the enhanced fracture strength of the brazed joint.

4.2. Mechanical contribution

One immediate question might arise as to whether the stress triaxiality associated with the mechanical constraint, can be used to reconcile the discrepancy between the calculated fracture strength of ~400 MPa and the experimental fracture stress of 478.7 ± 4.2 MPa, Table 1. For the 90° brazed joint that was under uniaxial tensile loading, both the base and filler metal would elongate in the longitudinal direction and contract in the transverse direction. However, plastic deformation of the joint would be restricted by the base metal due to elastic-plastic incompatibility, thereby introducing stress triaxiality. The stress state and deformation of brazed joints are therefore analogous to a specimen undergoes necking. As schematically shown in Fig. 12(a), upon necking, the uniaxial stress state is modified by the geometrically irregularity, leading to the presence of a triaxial stress state [45]. It then becomes important to derive the longitudinal flow stress after necking, i.e., correcting the experimentally obtained fracture stress.

For isotropic cylindrical specimens under tensile loading, Bridgman [46] formulated a geometric approximation to obtain the longitudinal flow stress σ_{TB} that accounts for the presence of the transverse components of stress σ_r and σ_θ, Fig. 12(a), assuming a uniform strain distribution in the minimum cross-section:

$$\sigma_{TB} = \sigma_T \left[\left(1 + \frac{2R}{a} \right) \ln \left(1 + \frac{a}{2R} \right) \right]^{-1} \qquad (5)$$

where σ_T represents the true flow stress prior to applying the Bridgman correction, a is the internal radius of the tensile specimen at the minimum cross section, and R is the radius of the external curvature of the necking profile as indicated in Fig. 12(b). Although the Bridgman necking criteria was developed for cylindrical specimens, Zhang et al. [47] confirmed that it can be used for specimens with rectangular shape and the correction of longitudinal flow stress was independent of the cross-section aspect ratio.

In this work, the true flow stresses σ_T at sample fracture of the brazed joints was calculated firstly by considering the reduced cross-sectional area as measured from the fracture surfaces. Measurement of the thickness and width before (W & L) and after (W' & L') tensile failure was performed on three tensile specimens. The average values were calculated and are given in Table 2. Note, the average Bridgman necking parameters are also listed in Table 2. To this end, the average width of tensile specimens reduced from 5.92 mm (W) to 4.95 mm (W') and the thickness reduced from 2.94 mm (L) to 2.45 mm (L'). The true flow stress at sample fracture σ_T was thus determined as 687.7 MPa, Table 2.

The Bridgman necking parameter R was measured from the fractured tensile specimens as shown in Fig. 12(c), where the circle represents the external curvature in the necking region and its radius was considered as the R values. The average value of R derived from Z-X plane was 0.20 mm, Table 2. To ensure the accuracy of R, Zhang et al. [48] proposed to verify the deformed cross sections by performing interrupted tensile tests. Therefore, the external curvature radius of specimens that had been strained to 90% of the fracture stresses was also examined. The radius values ranged from ~0.20 mm to ~0.30 mm when observing on Z-X plane, Fig. 12(d).

It is thus confirmed that the Bridgman necking parameter R determined from the failed specimen (0.20 mm, Table 2) is reliable. The Bridgman necking parameter a (internal radius at the minimum cross section) was taken as half of the width of the specimen after tensile failure, i.e. a was taken as 1.22 mm when observing on Z-X plane. Thus, Eq. (5) was adopted to derive the longitudinal flow stress σ_{TB}, which was 367.6 MPa, Table 2. Similarly, σ_{TB} for Z-Y plane was calculated as 359.3 MPa, Table 2. To this end, σ_{TB} derived from Z-X and Z-Y planes are
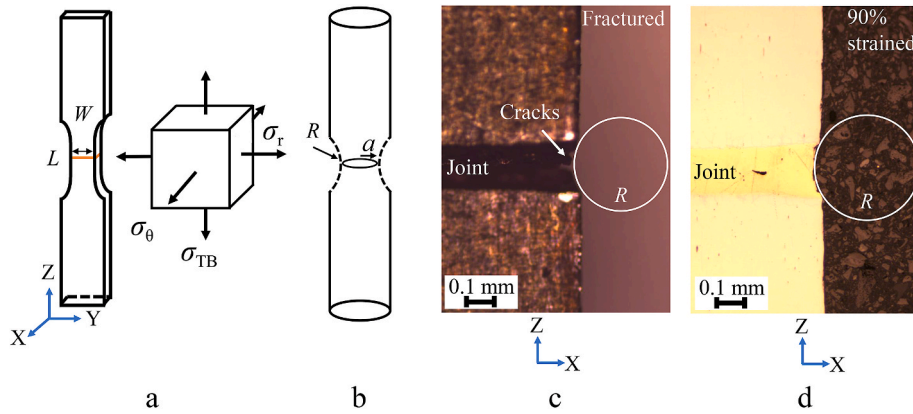
Fig. 12. (a) Illustration of specimen width and thickness, as well as stress triaxiality; (b) Bridgman necking parameters R and a; (c) determination of R on Z-X plane; (d) R values for specimens strained to 90% of the fracture stress.

Table 2
Average and standard deviation (STDEV) of thickness and width of specimens before (W & L) and after (W' & L') tensile failure; Bridgman necking parameters of the internal radius a and external curvature radius R observed on Z-X and Z-Y planes.

	Specimen width & thickness (mm)						Bridgman necking parameters (mm)					
		Before loading		After failure			Z-X plane			Z-Y plane		
	σ_f	W	L	W'	L'	σ_T	a	R	σ_{TB}	a	R	σ_{TB}
Average	478.7	5.92	2.94	4.95	2.45	687.7	1.22	0.20	367.6	2.48	0.37	359.3
STDVE	4.2	0.02	0.05	0.04	0.04	11.6	0.02	0.02	8.1	0.02	0.02	4.7

similar and the average value is taken as ~360 MPa.

The longitudinal flow stress σ_{TB} of ~360 MPa suggests that the brazed joints would fail at a much lower stress level without the help of mechanical constraint. This value is only slightly lower than the theoretical fracture strength of ~400 MPa based on Cu–Mn solid-solution contribution. Hence, it is judged that the longitudinal flow stress σ_{TB} at sample fracture agrees reasonably well with the theoretical joint strength. In addition, difference between the longitudinal flow stress σ_{TB} (~360 MPa) and the true flow stress σ_T at sample fracture (~690 MPa) is considered as the contribution of mechanical constraint, i.e. ~330 MPa. Therefore, the enhanced tensile strength of brazed joints can be considered as a combined effect of microscopic Cu–Mn solid-solution strengthening and macroscopic mechanical constraint effect.

4.3. Microscopic explanation for mechanical constraint

By creating the 45° brazed joint configuration (base-filler metal interface at 45° with respect to the loading axis), the level of mechanical constraint was reduced (lower stress triaxiality). To provide a microscopic explanation to the mechanical constraint, it is important to examine the GND distribution across the brazed joints. GND distribution was calculated for the 90° and 45° joint configurations for the as-brazed and strained condition. The kernel average misorientation (KAM) method was used to determine the local misorientation. Using continuum dislocation mechanics developed by Nye and Kroner [16], the dislocation density can be related to the lattice curvature assuming neglectable elastic strain. Note that EBSD-based dislocation analysis
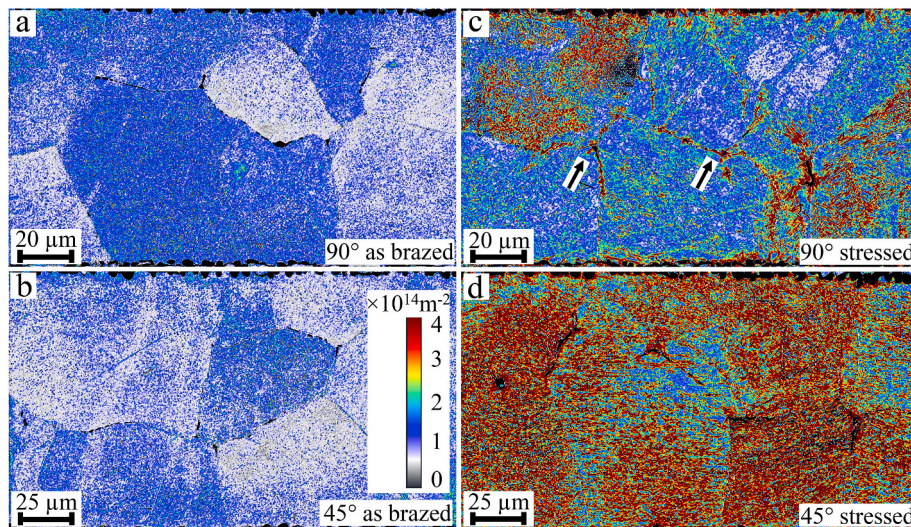

Fig. 13. (a) and (b) GND distributions within the 90° and 45° joints for the as-brazed condition; (c) and (d) GND distributions for the strained condition. It is advised to refer to Fig. 14 for a clearer reading of GND density.

considers GNDs only [49]. This is because GNDs are associated with long-range lattice curvature, whereas statistically stored dislocations are in the form of tangles without a net Burgers vector [28]. It is also realised that GND density derived from EBSD varies with step size [50]. Hence, the step size for EBSD scans in the current work was kept as 0.25 μm to minimise the measurement error.

Fig. 13 shows the derived GND density within the 90° and 45° joints for the as-brazed, Fig. 13(a) and (b), and the strained condition, Fig. 13 (c) and (d). The overall GND density was relatively low at as-brazed condition, being 1.0×10^{14} m^{-2} for both joint configurations, Fig. 13 (a) and (b). For the 90° joint at strained condition, high GND density was observed for certain grains that were favourably orientated, Fig. 13(c). This is consistent with the dislocation contrast observation for the 90° joint, Fig. 10(a). In addition, GND density was higher near grain boundaries and triple junctions, see arrows in Fig. 13(c), with a lower GND density within grain interiors. These observations comply with Ashby's theory [51] that GNDs are generated to ensure lattice continuity [8]. For the 45° joint at strained condition, Fig. 13(d), GND density was uniformly distributed across the joint region, supporting homogeneous dislocation contrast in Fig. 10(d).

To provide a quantitative measure of GND distribution, in particular near the base-filler metal interface, the average GND density was derived at different distances to the interface as shown in Fig. 14. For the as-brazed joint, GND density (circular symbols) was 1.0×10^{14} m^{-2} for both 90° and 45° configurations, confirming no GND gradient near the interfaces at as-brazed condition. At 90% strained condition, the 45° joint (hollow symbols) showed high GND density of 3.0×10^{14} m^{-2} across the joint region without much fluctuations. In contrast, GND gradient was clearly revealed for the 90° joint (black triangular), being 2.5×10^{14} m^{-2} in the vicinity of the interface and 1.7×10^{14} m^{-2} at locations away from the interface, Fig. 14.

The GND gradient in the 90° joint confirms the presence of elastic-plastic incompatibility between the base and filler metal imposed by the mechanical constraint. In other words, GNDs were introduced to accommodate inhomogeneous plastic deformation as a consequence of mechanical constraint. In contrast, uniform GND distribution in the 45° joint proves a reduced mechanical constraint effect. This agrees with our findings of smaller GNB spacings and lower tensile strength for the 45° brazed joints.

Previous work [23] demonstrated that the overall strain hardening behaviour of copper/bronze laminate materials, with improvements in both strength and ductility, can be associated with the role of interfaces. Mechanistically, the property enhancement is a result of the geometric discontinuity of slip systems across the interfaces [52]. Lee et al. [53] suggested that strain gradient could occur due to inhomogeneous plastic deformation, which needs to be accommodated by GNDs at the inter-phase boundaries. The pile-up of GNDs would generate back-stresses that countervail the forward motion of dislocations and therefore counterbalance the applied stress, leading to enhanced strength and ductility [54,55]. Thus, the GND pile-up at the base-filler metal interfaces as observed in the present brazed joint is considered as micro-scopic evidence for strain inhomogeneity due to the presence of mechanical constraint. Investigation of the back-stress effect will be conducted in the future. This will include evaluation of back-stress hardening effect by analysing the stress-strain hysteresis loop on the basis of the unloading-reloading type of tensile testing, as detailed in Refs. [56]. In addition, GND calculation will be performed for the joint region as well as the base metal region.

In summary, the enhanced mechanical strength of brazed joints is a concurrent result of (i) Cu–Mn solid-solution strengthening, (ii) mechanical constraint. The mechanical constraint is a macroscopic effect, that is caused by elastic-plastic incompatibility between the base stainless steel and copper-rich joint region, Fig. 15(a). The mechanical constraint can be characterised via the Bridgman necking criteria and is present in brazed joints regardless of the specific material system. In contrast, the Cu–Mn solid-solution strengthening can be considered as a microscopic contribution. Material strength of a brazed joint can be estimated by considering the intrinsic strength of the filler metal (i.e. pure Cu in the current work) and additional strengthening caused by the inter-diffusion of elements. This microscopic contribution is material dependent and can be modified by changing the processing parameters. Furthermore, the GND pile-up at the base-filler metal interface provides an experimental (microscopic) evidence for strain inhomogeneity imposed by the mechanical constraint, as schematically illustrated in Fig. 15(b). Based on this finding, strain heterogeneity study in the vicinity of the base-filler metal interfaces within the brazed joints, by conducting in-situ tensile testing coupled with digital image correlation technique, will be our future work.

5. Conclusions

This paper elucidates the microscopic and macroscopic material strengthening mechanism encountered in brazed joints. The following conclusions can be made:

1. The enhanced tensile strength of the brazed joint is a combined consequence of mechanical constraint and Cu–Mn solid-solution strengthening.
2. The Cu–Mn solid-solution strengthening leads to a tensile strength enhancement of ~200 MPa. By comparison, both the grain size and precipitation hardening played limited role.
3. The mechanical constraint presented in the 90° joint leads to an increased fracture strength, the calculation of longitudinal flow stress via the Bridgman necking criteria suggests a contribution of ~330 MPa. The mechanical constraint is responsible for reconciling the discrepancy between the calculated and experimentally determined strengths.
4. GND gradient was confirmed for the 90° joint, being 2.5×10^{14} m^{-2} near the interface and 1.7×10^{14} m^{-2} in the joint centre, whereas a homogeneous GND density of 3.0×10^{14} m^{-2} was found for the 45° joint. The pile-up of GNDs at the base-filler metal interface provides an experimental (microscopic) evidence for strain inhomogeneity imposed by the mechanical constraint.
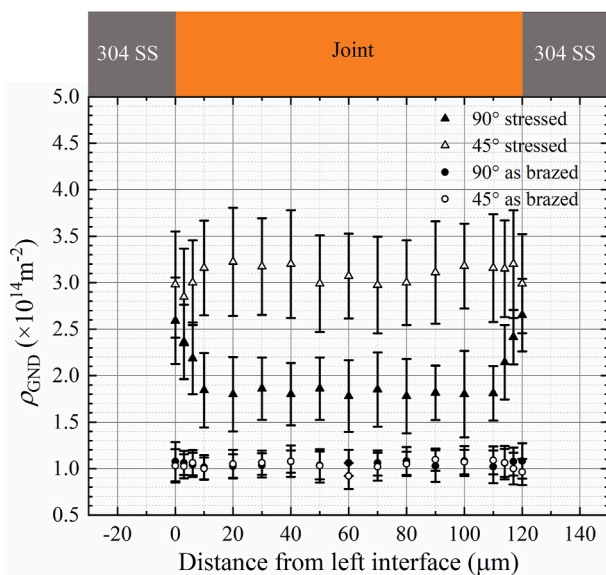

Fig. 14. Average GND densities within the 45° and 90° brazed joints at different distances to the base-filler metal interface.

Data availability

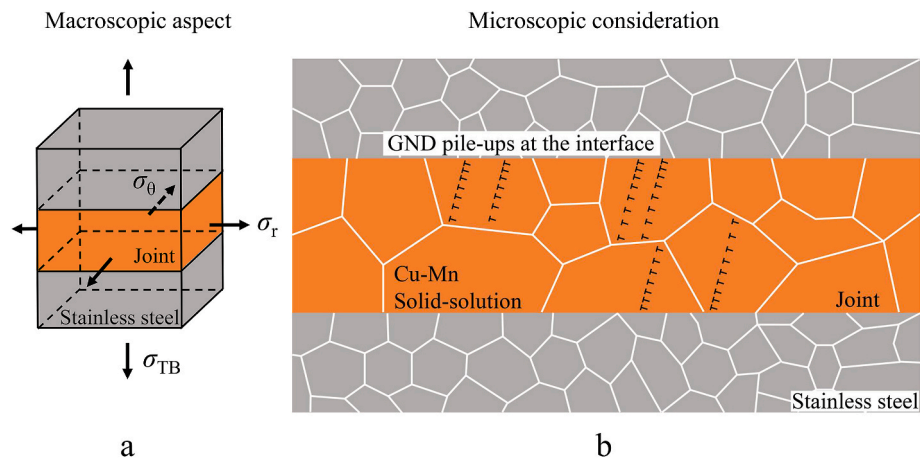The raw/processed data required to reproduce these findings cannot

Fig. 15. (a) Mechanical constraint and induced stress triaxiality in 90° brazed joint; (b) schematic illustration of Cu–Mn solid-solution strengthening and the pile-up of GNDs at the base-filler metal interface.

be shared at this time due to technical or time limitations.

CRediT authorship contribution statement

Y. Li: Conceptualization, Writing - original draft, Visualization. **D. Parfitt:** Investigation, Supervision, Writing - review & editing. **P.E.J. Flewitt:** Writing - review & editing. **X. Hou:** Investigation, Resources. **J. Quinta de Fonseca:** Writing - review & editing. **B. Chen:** Conceptualization, Supervision, Writing - review & editing.

Declaration of competing interest

The authors declare that they have no known competing financial interests or personal relationships that could have appeared to influence the work reported in this paper.

Acknowledgement

Appendix A. Supplementary data

Supplementary data to this article can be found online at https://doi.org/10.1016/j.msea.2020.139992.

References

[1] F. Silze, G. Wiehl, I. Kaban, H. Wendrock, T. Gemming, U. Kühn, J. Eckert, S. Pauly, Wetting behaviour of Cu-Ga alloys on 304L steel, Mater. Des. 91 (2016) 11–18.

[2] R.K. Roy, A.K. Panda, S.K. Das, Govind, A. Mitra, Development of a copper-based filler alloy for brazing stainless steels, Mater. Sci. Eng. 523 (2009) 312–315.

[3] F.P.L. Kavishe, T.J. Baker, Influence of joint gap width on strength and fracture toughness of copper brazed steels, Mater. Sci. Technol. 6 (1990) 176–181.

[4] A.J. West, H.J. Saxton, A.S. Telelman, C.R. Barrett, Deformation and failure of thin brazed joints-microscopic considerations, Metall. Mater. Trans. B Process Metall. Mater. Process. Sci. 2 (1971) 1009–1017.

[5] H.J. Saxton, A.J. West, C.R. Barrett, Deformation and failure of brazed joints-macroscopic considerations, Metall. Mater. Trans. B Process Metall. Mater. Process. Sci. 2 (1971) 999–1007.

[6] M.K. Ghovanlou, H. Jahed, A. Khajepour, Mechanical reliability characterization of low carbon steel brazed joints with copper filler metal, Mater. Sci. Eng. 528 (2011) 6146–6156.

[7] J. Kadkhodapour, S. Schmauder, D. Raabe, S. Ziaei-Rad, U. Weber, M. Calcagnotto, Experimental and numerical study on geometrically necessary dislocations and non-homogeneous mechanical properties of the ferrite phase in dual phase steels, Acta Mater. 59 (2011) 4387–4394.

[8] J. Jiang, T.B. Britton, A.J. Wilkinson, Evolution of dislocation density distributions in copper during tensile deformation, Acta Mater. 61 (2013) 7227–7239.

[9] X.W. Zhang, J.F. Wen, X.C. Zhang, X.G. Wang, S.T. Tu, Effects of the stress state on plastic deformation and ductile failure: experiment and numerical simulation using a newly designed tension-shear specimen, Fatig. Fract. Eng. Mater. Struct. 42 (2019) 2079–2092.

[10] W. Li, F. Liao, T. Zhou, H. Askes, Ductile fracture of Q460 steel: effects of stress triaxiality and Lode angle, J. Constr. Steel Res. 123 (2016) 1–17.

[11] Y. Li, X. Zhang, D. Parfitt, S. Jones, B. Chen, Characterisation of microstructure, defect and high-cycle-fatigue behaviour in a stainless steel joint processed by brazing, Mater. Char. 151 (2019) 542–552.

[12] X. Hou, N.M. Jennett, Application of a modified slip-distance theory to the indentation of single-crystal and polycrystalline copper to model the interactions between indentation size and structure size effects, Acta Mater. 60 (2012) 4128–4135.

[13] W.C. Oliver, G.M. Pharr, An improved technique for determining hardness and elastic modulus using load and displacement sensing indentation experiments, J. Mater. Res. 7 (1992) 1564–1583.

[14] B. Chen, J.N. Hu, P.E.J. Flewitt, A.C.F. Cocks, R.A. Ainsworth, D.J. Smith, D. W. Dean, F. Scenini, Effect of thermal ageing on creep and oxidation behaviour of Type 316H stainless steel, Mater. A. T. High. Temp. 32 (2015) 592–606.

[15] B. Beausir, J.-J. Fundenberger, Analysis Tools for Electron and X-Ray Diffraction, ATEX - software, 2017. www.atex-software.eu.

[16] J.F. Nye, Some geometrical relations in dislocated crystals, Acta Metall. 1 (1953) 153–162.

[17] B. Chen, P.E.J. Flewitt, D.J. Smith, C.P. Jones, An improved method to identify grain boundary creep cavitation in 316H austenitic stainless steel, Ultramicroscopy 111 (2011) 309–313.

[18] T. Ogura, S. Hirosawa, A. Cerezo, T. Sato, Atom probe tomography of nanoscale microstructures within precipitate free zones in Al-Zn-Mg(-Ag) alloys, Acta Mater. 58 (2010) 5714–5723.

[19] K. Chen, X. Chen, D. Ding, G. Shi, Z. Wang, Crystallographic features of iron-rich nanoparticles in cast Cu-10Sn-2Zn-1.5Fe-0.5Co alloy, Mater. Char. 113 (2016) 34–42.

[20] T. Grosdidier, A. Hazotte, A. Simon, Precipitation and dissolution processes in γ/γ′ single crystal nickel-based superalloys, Mater. Sci. Eng. 256 (1998) 183–196.

[21] X. Fan, Z. Guo, X. Wang, J. Yang, J. Zou, Morphology evolution of γ′ precipitates in a powder metallurgy Ni-base superalloy, Mater. Char. 139 (2018) 382–389.

[22] X.D. Hou, A.J. Bushby, N.M. Jennett, Study of the interaction between the indentation size effect and Hall-Petch effect with spherical indenters on annealed polycrystalline copper, J. Phys. D Appl. Phys. 41 (2008).

[23] X. Ma, C. Huang, J. Moering, M. Ruppert, H.W. Höppel, M. Göken, J. Narayan, Y. Zhu, Mechanical properties of copper/bronze laminates: role of interfaces, Acta Mater. 116 (2016) 43–52.

[24] E.J. Pavlina, C.J. Van Tyne, Correlation of Yield strength and Tensile strength with hardness for steels, J. Mater. Eng. Perform. 17 (2008) 888–893.

[25] Y. Chen, X. Zhang, E. Liu, C. He, C. Shi, J. Li, P. Nash, N. Zhao, Fabrication of in-situ grown graphene reinforced Cu matrix composites, Sci. Rep. 6 (2016) 1–9.

[26] Q. Liu, D. Juul Jensen, N. Hansen, Effect of grain orientation on deformation structure in cold-rolled polycrystalline aluminium, Acta Mater. 46 (1998) 5819–5838.

[27] D.A. Hughes, N. Hansen, Microstructure and strength of nickel at large strains, Acta Mater. 48 (2000) 2985–3004.

[28] C. Moussa, M. Bernacki, R. Besnard, N. Bozzolo, Statistical analysis of dislocations and dislocation boundaries from EBSD data, Ultramicroscopy 179 (2017) 63–72.

[29] D.A. Hughes, N. Hansen, D.J. Bammann, Geometrically necessary boundaries, incidental dislocation boundaries and geometrically necessary dislocations, Scripta Mater. 48 (2003) 147–153.

[30] A. Godfrey, D.A. Hughes, Scaling of the spacing of deformation induced dislocation boundaries, Acta Mater. 48 (2000) 1897–1905.

[31] O.V.V. Mishin, D. Juul Jensen, N. Hansen, D.J. Jensen, N. Hansen, Microstructures and boundary populations in materials produced by equal channel angular extrusion, Mater. Sci. Eng. 342 (2003) 320–328.

[32] D.A. Hughes, N. Hansen, High angle boundaries formed by grain subdivision mechanisms, Acta Mater. 45 (1997) 3871–3886.

[33] J.Y. He, H. Wang, H.L. Huang, X.D. Xu, M.W. Chen, Y. Wu, X.J. Liu, T.G. Nieh, K. An, Z.P. Lu, A precipitation-hardened high-entropy alloy with outstanding tensile properties, Acta Mater. 102 (2016) 187–196.

[34] L. Peng, H. Xie, G. Huang, G. Xu, X. Yin, X. Feng, X. Mi, Z. Yang, The phase transformation and strengthening of a Cu-0.71 wt% Cr alloy, J. Alloys Compd. 708 (2017) 1096–1102.

[35] G. Shi, X. Chen, H. Jiang, Z. Wang, H. Tang, Y. Fan, Strengthening mechanisms of Fe nanoparticles for single crystal Cu-Fe alloy, Mater. Sci. Eng. 636 (2015) 43–47.

[36] K.R. Anderson, J.R. Groza, Microstructural size effects in high-strength high-conductivity Cu-Cr-Nb alloys, Metall. Mater. Trans. A Phys. Metall. Mater. Sci. 32 (2001) 1211–1223.

[37] Y.J. Li, A.M.F. Muggerud, A. Olsen, T. Furu, Precipitation of partially coherent α-Al (Mn,Fe)Si dispersoids and their strengthening effect in AA 3003 alloy, Acta Mater. 60 (2012) 1004–1014.

[38] F. Qian, S. Jin, G. Sha, Y. Li, Enhanced dispersoid precipitation and dispersion strengthening in an Al alloy by microalloying with Cd, Acta Mater. 157 (2018) 114–125.

[39] Y.Y. Zhao, H.W. Chen, Z.P. Lu, T.G. Nieh, Thermal stability and coarsening of coherent particles in a precipitation-hardened (NiCoFeCr)94Ti2Al4 high-entropy alloy, Acta Mater. 147 (2018) 184–194.

[40] A. Sengupta, S.K. Putatunda, L. Bartosiewicz, J. Hangas, P.J. Nailos, M. Peputapeck, F.E. Alberts, Tensile behavior of a new single crystal nickel-based superalloy (CMSX-4) at room and elevated temperatures, J. Mater. Eng. Perform. 3 (1994) 664–672.

[41] R.E. Smallman, A.H.W. Ngan, Modern Physical Metallurgy, eighth ed., 2014. Oxford, UK.

[42] Z.C. Cordero, B.E. Knight, C.A. Schuh, Six decades of the Hall–Petch effect – a survey of grain-size strengthening studies on pure metals, Int. Mater. Rev. 61 (2016) 495–512.

[43] C.A. Schuh, T.G. Nieh, H. Iwasaki, The effect of solid solution W additions on the mechanical properties of nanocrystalline Ni, Acta Mater. 51 (2003) 431–443.

[44] J.Y. He, W.H. Liu, H. Wang, Y. Wu, X.J. Liu, T.G. Nieh, Z.P. Lu, Effects of Al addition on structural evolution and tensile properties of the FeCoNiCrMn high-entropy alloy system, Acta Mater. 62 (2014) 105–113.

[45] J.M. Choung, S.R. Cho, Study on true stress correction from tensile tests, J. Mech. Sci. Technol. 22 (2008) 1039–1051.

[46] P.W. Bridgman, Studies in Large Plastic Flow and Fracture, 1964.

[47] Z.L. Zhang, M. Hauge, J. Ødegård, C. Thaulow, Determining material true stress-strain curve from tensile specimens with rectangular cross-section, Int. J. Solid Struct. 36 (1999) 3497–3516.

[48] Z.L. Zhang, J. Ødegård, O.P. Søvik, Determining true stress-strain curve for isotropic and anisotropic materials with rectangular tensile bars: method and verifications, Comput. Mater. Sci. 20 (2001) 77–85.

[49] T.J. Ruggles, T.M. Rampton, A. Khosravani, D.T. Fullwood, The effect of length scale on the determination of geometrically necessary dislocations via EBSD continuum dislocation microscopy, Ultramicroscopy 164 (2016) 1–10.

[50] E. Demir, D. Raabe, N. Zaafarani, S. Zaefferer, Investigation of the indentation size effect through the measurement of the geometrically necessary dislocations beneath small indents of different depths using EBSD tomography, Acta Mater. 57 (2009) 559–569.

[51] M.F. A, The deformation of plastically non-homogeneous materials, Philos. Mag. A 21 (1969) 37–41.

[52] N. Li, J. Wang, J.Y. Huang, A. Misra, X. Zhang, In situ TEM observations of room temperature dislocation climb at interfaces in nanolayered Al/Nb composites, Scripta Mater. 63 (2010) 363–366.

[53] H.H. Lee, J.I. Yoon, H.K. Park, H.S. Kim, Unique microstructure and simultaneous enhancements of strength and ductility in gradient-microstructured Cu sheet produced by single-roll angular-rolling, Acta Mater. 166 (2019) 638–649.

[54] X. Wu, Y. Zhu, Heterogeneous materials: a new class of materials with unprecedented mechanical properties, Mater. Res. Lett. 5 (2017) 527–532.

[55] C.W. Shao, P. Zhang, Y.K. Zhu, Z.J. Zhang, Y.Z. Tian, Z.F. Zhang, Simultaneous improvement of strength and plasticity: additional work-hardening from gradient microstructure, Acta Mater. 145 (2018) 413–428.

[56] M. Yang, Y. Pan, F. Yuan, Y. Zhu, X. Wu, Back stress strengthening and strain hardening in gradient structure, Mater. Res. Lett. 4 (2016) 145–151.